Christian Rhode*, Finn Bietz, Thorsten M. Gesing, Christopher S. Reuter, Pia Maria Düring, Martina Müller, Ramazan Koc, Darrell G. Schlom, Yilin Evan Li, Matthias Bickermann, Simone Sanna and Christo Guguschev

Understanding structure and structural formation in Mg & Zr-substituted $Sr(Ga_{12-x}Al_x)O_{19}$-crystals. A study combining X-ray diffraction and DFT-modeling

https://doi.org/10.1515/zkri-2026-0009
Received February 20, 2026; accepted May 28, 2026;
published online August 10, 2026

Abstract: The crystal structure of Mg and Zr- substituted strontium-hexagallate/-aluminate $Sr(Ga_{12-x}Al_x)O_{19}$ single crystals is investigated by combining single crystal diffraction and quantum mechanical modeling based on density functional theory (DFT). The crystal structure is solved within the magnetoplumbite structure type (space group $P6_3/mmc$, $Z = 2$). Moreover, a refinement is carried out to determine the Wyckoff sites occupied by the substituent atoms Mg and Zr, as well as the shared occupancy of Ga and Al in the $Sr(Ga_{12-x}Al_x)O_{19}$ solid solution. Through DFT calculations, the formation energies for the introduction of Mg, Zr and Al into the structure are determined, thus revealing the energetically most preferred sites for these cations. Both methods show results which are in good agreement, thus corroborating each other and providing the basis for a deepened understanding of the material in question.

Keywords: single crystal diffraction; density functional theory; structural modeling; crystal structure determination; magnetoplumbite structure type

***Corresponding author: Christian Rhode**, Leibniz-Institut für Kristallzüchtung, Max-Born-Straße 2, 12489 Berlin, Germany, E-mail: christian.rhode@ikz-berlin.de
Finn Bietz and Simone Sanna, Institut für theoretische Physik, Justus-Liebig-Universität Gießen, Heinrich-Buff-Ring 16, 35392 Gießen, Germany
Thorsten M. Gesing, Institut für anorganische Chemie und Kristallographie/FB02, Universität Bremen, Leobener Straße 7, 28359 Bremen, Germany; and MAPEX Center for Materials and Processes, Bibliothekstraße 1, D-28359 Bremen, Germany
Christopher S. Reuter, Institut für anorganische Chemie und Kristallographie/FB02, Universität Bremen, Leobener Straße 7, 28359 Bremen, Germany
Pia Maria Düring and Martina Müller, Fachbereich Physik, Universität Konstanz, Universitätsstraße 10, 78464 Konstanz, Germany
Ramazan Koc, Matthias Bickermann and Christo Guguschev, Leibniz-Institut für Kristallzüchtung, Max-Born-Straße 2, 12489 Berlin, Germany
Darrell G. Schlom, Leibniz-Institut für Kristallzüchtung, Max-Born-Straße 2, 12489 Berlin, Germany; Department of Materials Science and Engineering, Cornell University, Ithaca, NY 14853-1501, USA; and Kavli Institute at Cornell for Nanoscale Science, Ithaca, NY 14853, USA
Yilin Evan Li, Department of Materials Science and Engineering, Cornell University, Ithaca, NY 14853-1501, USA

The precise control of the lattice parameters of epitaxially grown materials is required both for the realization of nearly defect-free structures as well as for tuning material properties via strain engineering. Unfortunately, one major issue in materials engineering is the limited availability of substrates for the lattice matched growth of thin films and nanostructures.[1–4] The substrate shortage is particularly severe in the case of materials crystallizing in the hexagonal magnetoplumbite structure (Space group: $P6_3/mmc$), which includes, among others, different hexaferrites with appealing ferrimagnetic and potentially ferroelectric properties (through strain engineering).[5–10]

In this context, magnetoplumbite crystalline type substrates with lattice parameters adjustable by chemical substitution (the so called next-generation substrates) are very valuable. Among these compounds, strontium-aluminum hexagallate $Sr(Ga_{12-x}Al_x)O_{19}$ is a solid solution with lattice parameters that decrease with increasing Al content.[11] Moreover, substituting Ga with different transition metals such as Zr and Mg can be used to further tune the structural parameters, providing a further opportunity for active strain engineering.[12]

Thus, while the commercial unavailability of isostructural substrates has been a fundamental limitation for the growth of high-quality epitaxial films of hexaferrites,[13] $Sr(Ga_{12-x}Al_x)O_{19}$ has been recently used for the growth of multiferroic barium hexaferrite ($BaFe_{12}O_{19}$) films.[14] In this case, the chemical substitution of Ga by Al was used to reduce the lattice parameters and induce in-plane compressive strain in the $BaFe_{12}O_{19}$ thin films. The structural strain in the grown films enhances the displacement of the Fe ions from the high-symmetry position and is thus used to tune the magnitude of the ferroelectric polarization.[9,14]

Although the crystal structure of strontium hexagallate is known and it is generally accepted that Mg and Zr substitute Ga ions in $SrGa_{12}O_{19}$, no conclusive structural model for Mg, Zr substituted crystals is available from experimental or theoretical studies, and the exact lattice position of said substituents is not determined. Similarly, the site occupancy of Al in a $Sr(Ga_{12-x}Al_x)O_{19}$ solid solutions with varying Al concentrations have not yet been systematically investigated.

The study at hand attempts to close this knowledge gap. To elucidate the structure of Mg and Zr-substituted $Sr(Ga_{12-x}Al_x)O_{19}$-crystals, we combine the results of single crystal diffraction-based experiments and first-principles atomistic calculations. The lattice positions of the substituents derived from the diffraction experiments correspond to the minima of the defect formation energy as predicted by DFT. This allows a structural model to be proposed, including the positions of the Mg, Zr and Al ions in the structure of the solid solutions.

1 Crystallographic details

The $Sr(Ga_{12-x}Al_x)O_{19}$ solid solution crystallizes in the hexagonal space group $P6_3/mmc$ (magnetoplumbite structure) depicted in Figure 1. The lattice parameters of the end-members $SrGa_{12}O_{19}$ and $SrAl_{12}O_{19}$ are $\vec{a}$ = 5.7929(1) Å and $\vec{c}$ = 22.8123(7) Å[15] and $\vec{a}$ = 5.5718 Å and $\vec{c}$ = 22.012 Å,[16] respectively. The Al and Ga-atoms of the end-members of the $Sr(Ga_{12-x}Al_x)O_{19}$ solid solution are distributed over a total of five non-equivalent Wyckoff sites within the magnetoplumbite structure, whereas Sr only occupies one lattice site. The Wyckoff sites and their corresponding occupancies are reported in Table 1. Solid solutions obtained by substituting Mg and Zr for Ga in strontium hexagallate are referred to as SGMZ, substituting Mg and Zr for Ga in the solid solution ($Sr(Ga_{12-x}Al_x)O_{19}$) are referred to as SGAMZ.

2 Single-crystal growth

The growth of all SGMZ crystals was conducted as demonstrated in Ref. 17, following the procedure outlined by Ref. 18. As for SGAMZ, the preparation of the precursor materials was followed the same procedure as SGMZ. The crystal was grown under a flowing CO_2-atmosphere (Flow: 6 L/h) at a pulling rate of 0.35 mm/h and rotational speed of 10 rpm. Instead of using a seed crystal, crystallization was induced by contacting the melt with an Ir-rod. The grown crystals

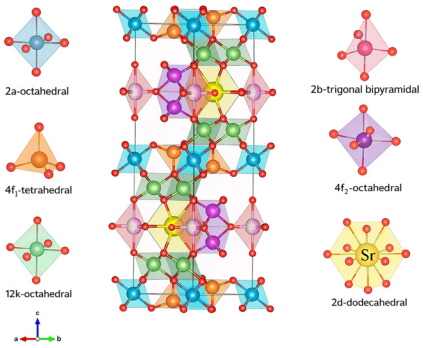

Figure 1: Graphic representation of the unit cell of general magnetoplumbite structure.

Table 1: Wyckoff positions with the respective occupancy for both $SrGa_{12}O_{19}$ and $SrAl_{12}O_{19}$. The coordination number **CN** indicates the number of neighboring oxygen atoms.

Element	Wyckoff site	CN	Point symmetry
Sr	*2d*	12	$\bar{6}m2$
Al/Ga	*2a*	6	$\bar{3}m$
Al/Ga	*2b*	5	$\bar{6}m2$
Al/Ga	$4f_1$	4	$3m$
Al/Ga	$4f_2$	6	$3m$
Al/Ga	*12k*	6	*m*

represented a multicrystalline aggregate comprised of a number of monocrystalline grains of different size.

3 Sample preparation and experimental details

A chemical pre-characterization of the grown crystals was conducted by ICP-OES. The obtained chemical information was used for fitting the obtained single crystal XRD data. For the XRD measurements, samples were prepared from single crystalline pieces from SGMZ and SGAMZ crystals. These were broken apart using an agate mortar. Suitable samples were selected under an optical microscope and mounted on polymer loops (*Jena Biocience*, 100 µm and 50 µm diameter) for measurement.

Single crystal X-ray diffraction (SCXRD) experiments were performed on two different D8 Venture systems (Bruker AXS GmbH, Karlsruhe, Germany). The apparatuses feature a KAPPA four-circle goniometer, a PHOTON 100 CMOS detector (100 cm^2 active area), and a curved graphite crystal TRIUMPH monochromator. Both employ $Mo_{K\alpha}$ radiation ($\lambda_{K\alpha1}$ = 70.93171(4) pm, $\lambda_{K\alpha2}$ = 71.3607(12) pm). The

machine used to measure the presented data pertaining SGAMZ is equipped with a Incoatec IμS Microsource tube. A complete data set was collected at room temperature, with a maximum resolution of 50 pm and a frame width of 0.5°. The SAINT software (Bruker AXS GmbH, Karlsruhe, Germany) was used for frame integration, and the intensities were corrected for absorption using a numerical method. The space group was determined by systematically examining absent reflections with the Xprep software as $P6_3/mmc$.[19] Structure solution and refinement were carried out using the SHELX software suite[19] implemented in OLEX2,[20] incorporating anisotropic displacement parameters for all sites, extinction, and the recommended weighting scheme during the final refinement steps.

4 HAXPES

To investigate the Zr:Mg-ratio of a (Mg,Zr):$SrGa_{12}O_{19}$ (SGMZ) single crystal, we carried out hard X-ray photoelectron spectroscopy (HAXPES) measurements at the P22 beamline of PETRA III (DESY, Hamburg).[21] Core level spectra of Zr, Mg, Sr, O and Ga were recorded at a photon energy of 2.8 keV, providing an information depth of about 13 nm. HAXPES is therefore more depth sensitive than conventional laboratory XPS (AlK_α or MgK_α), which is typically in the range of a few nanometers.[22] An SPECS PHOIBOS 225HV electron analyzer was used at an emission angle of 5° and a pass energy of 30 eV, resulting in an overall energy resolution of approximately 300 meV.[22]

5 Density functional theory

5.1 Convergence tests and computational procedure

The Vienna Ab initio Simulation Package (VASP) version 6.4.3,[23,24] employing the projector-augmented-wave (PAW) formalism,[25,26] was used for all calculations. The starting point of all calculations is the experimental structure of $SrGa_{12}O_{19}$, for which the equilibrium structure is calculated after converging the computational parameters. Both the cutoff energy and the k-points were optimized with respect to the total energy in a series of convergence tests. Plane waves up to a kinetic energy of 700 eV are considered in the basis set for the expansion of the electronic wave functions. The high value likely reflects the highly localized electrons of the fourth shell of Sr ions, necessitating an approach that uses high frequency plane waves. Due to the cell symmetry, a homogeneous k-point sampling can be obtained using a Monkhorst-Pack $(4\times4\times1)\cdot n$ k-point mesh.[27] As for values of $n \geq 2$ the total energy varies less than 10^{-3} meV, all calculations are performed with a $8\times8\times2$ k-point mesh. The atomic positions are determined minimizing the Hellmann-Feynman forces[28] below a threshold of 0.005 eV/Å. As an accurate description of the lattice parameters is crucial in the present investigation, different calculations performed describing the electron exchange and correlation interaction by the local density approximation (LDA) as parametrized by Perdew and Zunger[29] as well as the generalized gradient approximations (GGA) as parametrized by Perdew, Burke, and Ernzerhof (PBE),[30] by Perdew et al. (PBEsol)[31] are performed in the present work.

The structural parameters determined for $SrGa_{12}O_{19}$ within the different XC-functionals by fitting the Murnaghan state equation[32] are reported in Table 2, along with the deviation from the experimental values measured in this work. As usual, the LDA functional overestimates the strength of the atomic bonds, thus underestimating the lattice parameters. Vice versa, GGA based functional underestimate the bond strength and overestimate the lattice parameters. As LDA delivers the most accurate description of the experimental values, all the following calculations are performed within LDA.

5.2 Calculation of defect formation energies

The formation energies of the investigated defects are calculated within the dilute limit and the supercell approach as described in Ref. 33 according to

$$E^f[\chi^q] = E_{\text{tot}}[\chi^q] - E_{\text{tot}}[\text{Bulk}] - \sum_i n_i\mu_i + q[E_F + E_v + \Delta V]. \quad (1)$$

Table 2: Lattice parameters and volumes of $SrGa_{12}O_{19}$ calculated within DFT using different XC-functionals. The deviation is given with respect the lattice parameters of $SrGa_{12}O_{19}$ presented in Ref. 15.

	PBE	LDA	PBEsol
V_0 [Å^3]	702.42	659.59	681.42
V_0 deviation [%]	+5.95	−0.51	+2.79
$\vec{a} = \vec{b}$ [Å]	5.9159	5.7931	5.8564
$\vec{a} = \vec{b}$ deviation [%]	+2.12	−0.004	+1.10
$\vec{c}$ [Å]	23.1752	22.6942	22.9419
$\vec{c}$ deviation [%]	+1.59	−0.52	+0.57
$\vec{c}/\vec{a}$ ratio	3.9174	3.9174	3.9174
$\vec{c}/\vec{a}$ deviation [%]	0.52	0.52	0.52
Angle $\angle(\vec{a}, \vec{b})$	120°	120°	120°

Thereby $E_{tot}[\chi^q]$ is the total energy of a supercell containing the defect χ in the charge state q, E_{tot}[Bulk] is the total energy of an equivalent supercell of $SrGa_{12}O_{19}$ bulk. n_i is the number of species i that have been removed from ($n_i < 0$) or added to ($n_i > 0$) in the supercell to create the defect. μ_i is the chemical potentials of species i and represents the thermodynamical growth conditions. E_F is the Fermi level, which is given with respect to the valence-band maximum E_v. ΔV is a correction needed to align the potential in the supercell with the defect and in the bulk.

For the calculation of $E_{tot}[\chi^q]$, a supercell consisting of two strontium hexagallate unit cells along the shorter $\vec{a}$ -vectors and one unit cell along the $\vec{c}$ -vector are created to decouple the periodic images of the defects. Accordingly, the k-point sampling is reduced to ($4 \times 4 \times 2$). Subsequently, the substitutional defects involving Mg, Al or Zr were placed. This results in large supercells consisting of 256 atoms in which the defects are separated by more than 11 Å. Although a larger distance would be desirable to model the dilute limit, the chosen geometry represents a good compromise between accuracy and computational demand. As the relative formation energy of the same substitutional defect on different lattice sites and not the accurate estimate of their value is in the focus of the investigation, finite-size corrections for charged-defect supercell calculations[33,34] are not considered.

A series of structures was constructed, each incorporating a single substitutional defect within one supercell. These configurations included either the replacement of the Sr atom at the A site by Mg, Al, or Zr, or the substitution of one Ga atom at one of the five trivalent crystallographically non-equivalent sites listed in Table 1 by the same set of substituent elements. This results in a total of 18 distinct defect configurations. According to the experimental evidence, only isovalent substitutions of the Sr^{2+} and Ga^{3+} ions leading to the observed dopant charge state Al^{3+}, Mg^{2+} and Zr^{4+}) were considered.

Equation (1) shows that the defect formation energy depends both on the value of the chemical potentials and on the position of the Fermi energy. The chemical potential can assume different values within a stability range depending on the growth conditions. An upper bound is given by the metallic phase of the considered species (e.g., $\mu_{Ga} = \mu_{Ga}$[Bulk]), while a lower bound is given by oxygen rich conditions. Values of μ_i beyond these bounds will lead to the precipitation of the metallic phases or the formation of the respective oxides and not to the doped solid solutions considered in this work.

According to the experimental growth conditions, in which the crystals are pulled from a melt created by the oxidic phases, we chose oxygen-rich conditions as a reference for the calculation of the defect formation energy. The chemical potentials of the various elements are therefore calculated from their respective oxidic phase as listed in Table 3. Each considered compound is modeled within its unit cell after converging the computational parameter. The employed values are also reported in Table 3.

The position of the Fermi energy within the fundamental bandgap influences the absolute value of the defect formation energy. As it is experimentally known that the Fermi energy in all grown samples is roughly in the middle of the fundamental gap, the results that follow are calculated for a position of the Fermi energy arbitrarily chosen at 1 eV above the valence band maximum. A different choice will shift the calculated values of the formation energy of equally charged defects upwards or downwards. However, it will not affect their relative position and thus stability of the distinct lattice sites, whose estimate is the goal of the investigation. As no experimental evidence of dopants in different charge states than the investigated Al^{3+}, Mg^{2+} and Zr^{4+} exists, charge transition levels are not investigated in this work.

6 Results and discussion

6.1 Density functional theory

We start the presentation of our results with the theoretical predictions, which are later compared with the experimental results. Table 4 lists the formation energies of the considered defect centers calculated under oxygen-rich

Table 3: Oxidic reference phases used in the thermodynamical framework for the calculations of the chemical potentials within DFT. Computational parameters employed for the simulation of the compounds and calculated values of chemical potentials for oxygen rich conditions are given.

Element	Oxide	Atoms/UC	E_{cut} [eV]	k-points	μ_i [eV]
Sr	SrO	8 (4 Sr + 4 O)	500	(3 3 3)	−8.59
Ga	Ga_2O_3	20 (8 Ga + 12 O)	650	(2 8 4)	−10.01
Al	Al_2O_3	30 (12 Al + 18 O)	500	(6 6 2)	−13.60
Mg	MgO	8 (4 Mg + 4 O)	450	(3 3 3)	−8.66
Zr	ZrO_2	12 (4 Zr + 8 O)	450	(3 3 3)	−21.82
O	O_2			(1 1 1)	−9.54

Table 4: DFT calculated formation energies for the Al, Zr and Mg substituents on the different cation sites of the magnetoplumbite structure. The calculations model oxygen-rich thermodynamic conditions and midgap Fermi energy. Isovalent substitutions are considered.

Site	E^f_{Al} [eV]	E^f_{Mg} [eV]	E^f_{Zr} [eV]
2d	6.40	5.55	3.08
2a	2.99	4.86	3.42
2b	3.28	5.87	1.58
$4f_1$	3.42	4.70	2.33
$4f_2$	3.06	5.92	1.36
12k	3.06	5.39	2.68

conditions and midgap Fermi energy for the individual Wyckoff positions of the magnetoplumbite structure.

It is evident that Al, Mg, and Zr substitutional defects at the Sr lattice site are characterized by formation energies higher than those of substitutional defects at the Ga lattice site and are thus unlikely to occur. This fact can be traced back to the significantly larger Pauling ionic radius and lower Pauling electronegativity of Sr^{2+} (113 pm, 0.95 PU) compared to Mg^{2+} (65 pm, 1.31 PU), Al^{3+} (50 pm, 1.61 PU), and Zr^{4+} (80 pm, 1.33 PU).[35] These differences contribute to the consistently unfavorable defect formation energies observed for Sr substitution of all considered substituents. Interestingly, these considerations also hold for magnesium, despite its vicinity to strontium in the periodic table.

All investigated substituent atoms prefer the Ga lattice sites. Aluminum prefers the *2a* site followed by the $4f_2$ and *12k* sites, which correspond to the octahedral coordination. In contrast, substitutions at the *2b* and $4f_1$ sites (trigonal and tetrahedral coordination) are less favorable. The corresponding lattice sites are likely to be occupied only at high Al concentrations during growth. As a general rule, the substitution of gallium by aluminum results in relatively low formation energies of a few electronvolts, which is consistent with their chemical similarity (Ga^{3+} has a Pauling ionic radius of 62 pm and an electronegativity of 1.81 PU) though mirroring non-vanishing differences in size and electronegativity.

Substitution of Ga by Mg yields higher formation energies than substitutions by Al, in agreement with the greater disparity in size and electronegativity between Ga and Mg. For Magnesium, the $4f_1$ site with tetrahedral coordination has the lowest defect formation energy. Except for *2a*, the E^f of the remaining sites is notably higher.

The calculations for E^f_{Zr} yield somewhat lower values in comparison to those obtained for the other two substituents. The $4f_1$ site shows to be the energetically most stable for Zr with the other sites [with the exception of 2b] showing significantly higher energies by at least 1 eV.

6.2 Stoichiometry of a (Mg,Zr):$SrGa_{12}O_{19}$ single crystal

Core levels of every element were recorded by HAXPES to determine the chemical composition of the single crystal. Figure 2 displays the background corrected **(a)** Zr 3*d* core level and **(b)** Mg 2*s* core level measured at a photon energy of 2.8 keV. The core levels Zr 3*d* and Mg 2*s* were selected to determine the intensity ratio Zr:Mg, because they do not overlap with other elements or spectral features. Ideally, two or more core level per element are used to average over the intensity ratio. The stoichiometry was calculated from the Zr:Mg peak intensity ratio of Zr 3*d* and Mg 2*s* weighted by the respective photoionization cross sections[36,37] and results to a Zr:Mg ratio of 1:1.075 ± 0.15. Further details on the analytic model for stoichiometry determination can be found in Refs. 38,39. Although the amounts of Zr and Mg should be equal, the measurements reveal that the Mg content is slightly larger than the Zr content.

6.3 Single crystal diffraction

The crystal structure of both SGMZ and SGAMZ was determined from SCXRD-data. Based on the space group obtained during the processing of the measured data using XPREP, the structure was solved using SHLEXT whereas the successive refinement was carried out using SHELXL.[19] The obtained atomic parameters for both phases and the corresponding reliability factors are given in Tables 5 and 6.

The chemical formulas obtained through the fitting procedure are listed in Table 7, juxtaposed with the target composition and the results obtained from the ICP-OES.

Drawing from the results regarding the formation energies obtained through DFT-modeling (see Table 4), the structure was refined as such, that Mg and Zr share the tetrahedral $4f_1$ and the $4f_2$ sites with Ga respectively (see Table 5). The thus defined structural model yields the best fit results, especially after slight modification of the occupancies of the various Wyckoff-sites to reflect the stoichiometry as measured through ICP-OES. In comparison to the starting composition, the concentrations of Mg and Zr appear slightly more decreased as reported in Refs. 17,18 nevertheless reflecting the Mg/Zr-ratio as obtained through the HAXPES measurements (see Figure 2) well. As already observed in Ref. 18, the inclusion of Mg and Zr results in a slight increase of the lattice parameter of SGMZ in comparison to the unaltered $SrGa_{12}O_{19}$ ($\vec{a}$ = 5.7929(1) Å and $\vec{c}$ = 22.8123(7) Å[17]) and is in good agreement with reported values for SGMZ ($\vec{a}$ = 5.82364(4) Å and $\vec{c}$ = 23.07379(1) Å[17]).

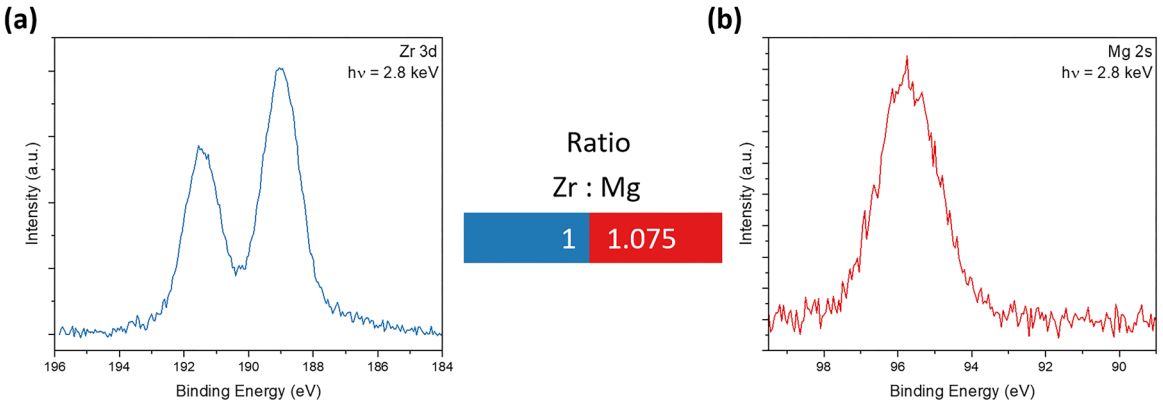

Figure 2: HAXPES spectra of (a) Zr 3*d* core level and (b) Mg 2*s* core level recorded at a photon energy of 2.8 keV. The spectra are background corrected to determine the ratio between both elements. The calculated intensity ratio weighted by the respective photoionization cross sections is displayed in the middle.

Table 5: SGMZ crystal structure as obtained by structure fitting using SHELXL. $U_{13} = U_{23} = 0$.

Symmetry	**Space group**	$\vec{a}$ **[Å]**	$\vec{c}$ **[Å]**	ρ [$\frac{g}{m^3}$]	M [$\frac{g}{mol}$]
Hexagonal	$P6_3/mmc$	5.81899(7)	23.0532(4)	5.632(4)	1,006.71(6)
Site	**Atom**	***x***	***y***	***z***	**Occ.**
2d	Sr	$\frac{2}{3}$	$\frac{1}{3}$	$\frac{1}{4}$	1.000
2a	Ga	0	0	0	1.000
2b	Ga	0	0	0.23594(6)	0.500
$4f_1$	Ga	$\frac{1}{3}$	$-\frac{1}{3}$	0.02668(4)	0.726(8)
$4f_1$	Mg	$\frac{1}{3}$	$-\frac{1}{3}$	0.02668(4)	0.274(4)
$4f_2$	Ga	$\frac{1}{3}$	$\frac{2}{3}$	0.18824(3)	0.745(1)
$4f_2$	Zr	$\frac{1}{3}$	$\frac{2}{3}$	0.18824(3)	0.255(7)
12k	Ga	0.33622(8)	0.16811(4)	0.10720(2)	1.000
Site	**Atom**	U_{11}	U_{22}	U_{33}	U_{12}
2d	Sr	0.0154(3)	0.0154(3)	0.0115(4)	0.00772(17)
2a	Ga	0.0063(3)	0.0063(3)	0.0059(4)	0.00317(16)
2b	Ga	0.0039(4)	0.0039(4)	0.0108(8)	0.00196(19)
$4f_1$	Ga	0.0012(3)	0.0012(3)	0.0021(4)	0.00058(14)
$4f_1$	Mg	0.0012(3)	0.0012(3)	0.0021(4)	0.00058(14)
$4f_2$	Ga	0.0039(3)	0.0039(3)	0.0086(4)	0.00195(13)
$4f_2$	Zr	0.0039(3)	0.0039(3)	0.0086(4)	0.00195(13)
12k	Ga	0.0034(3)	0.0045(2)	0.0061(2)	0.00170(13)
R_{int}	R_1	wR_2	**GoF**	**Highest peak**	**Deepest hole**
3.60 %	2.06 %	6.38 %	1.150	1.1 $e^-/Å^3$	−2.0 $e^-/Å^3$
h, k, l	**Reflections collected**	**Unique reflections**			
−-8 -8 -32 −8 832	28.013	452			

As for SGAMZ, Mg and Zr are again placed on the $4f_1$ and $4f_2$ sites. At the given stoichiometry, Al occupies the *2a* Octahedral and the *12k* octahedral site. Here, the *2a* octahedral site is noticeably stronger populated by Al than the *12k* site (see Table 6). This again agrees well with the formation energy of the respective site being the lowest, thus making it the energetically most attractive site to be occupied by Al. The Al-occupancy on the *2a* and *12k* octahedral

Table 6: SGAMZ crystal structure as obtained by structure fitting using SHELXL. $U_{13} = U_{23} = 0$.

Symmetry	Space group	$\hat{a}$ [Å]	$\hat{c}$ [Å]	ρ $[\frac{g}{m^3}]$	M $[\frac{g}{mol}]$
Hexagonal	$P6_3/mmc$	5.73640(14)	22.7824(8)	4.825(1)	961.18(3)
Site	**Atom**	***x***	***y***	***z***	**Occ.**
2d	Sr	$-\frac{1}{3}$	$\frac{1}{3}$	$\frac{1}{4}$	1.000
2a	Ga	0	0	0	0.313(3)
2a	Al	0	0	0	0.687(9)
2b	Ga	0	0	0.23571(7)	0.500
$4f_1$	Ga	$\frac{1}{3}$	$-\frac{1}{3}$	0.02690(4)	0.784(5)
$4f_1$	Mg	$\frac{1}{3}$	$-\frac{1}{3}$	0.02690(4)	0.216(7)
$4f_2$	Ga	$\frac{1}{3}$	$\frac{2}{3}$	0.18800(4)	0.798(1)
$4f_2$	Zr		$\frac{2}{3}$	0.18800(4)	0.202(8)
12k	Ga	0.33605(13)	0.16803(7)	0.10739(3)	0.586(6)
12k	Al	0.33605(13)	0.16803(7)	0.10739(3)	0.414(3)
Site	**Atom**	U_{11}	U_{22}	U_{33}	U_{12}
2d	Sr	0.0126(4)	0.0126(4)	0.0103(5)	0.00632(18)
2a	Ga	0.0044(8)	0.0044(8)	0.0047(9)	0.0022(4)
2a	Al	0.0044(8)	0.0044(8)	0.0047(9)	0.0022(4)
2b	Ga	0.0047(4)	0.0047(4)	0.0137(9)	0.0023(2)
$4f_1$	Ga	0.0018(3)	0.0018(3)	0.0034(4)	0.00090(16)
$4f_1$	Mg	0.0018(3)	0.0018(3)	0.0034(4)	0.00090(16)
$4f_2$	Ga	0.0077(3)	0.0077(3)	0.0114(4)	0.00386(16)
$4f_2$	Zr	0.0077(3)	0.0077(3)	0.0114(4)	0.00386(16)
12k	Ga	0.0052(4)	0.0062(3)	0.0085(4)	0.00258(19)
12k	Al	0.0052(4)	0.0062(3)	0.0085(4)	0.00258(19)
R_{int}	R_1	wR_2	GoF	Highest peak	Deepest hole
6.53 %	2.34 %	6.66 %	1.200	1.2 $e^-/Å^3$	−1.4 $e^-/Å^3$
h, k, l	**Reflections collected**	**Unique reflections**			
-8-8-32 –8 8 32	21.627	439			

Table 7: Comparison of crystal compositions as obtained through the XRD-experiments or chemical analysis with the initial composition of the melt.

	SGMZ	SGAMZ
Melt	$Sr_{1.56}Ga_{10.40}Mg_{0.52}Zr_{0.52}O_{19}$	$Sr_{1.45}Ga_{7.92}Al_{2.61}Mg_{0.52}Zr_{0.52}O_{18.77}$
XRD	$SrGa_{10.94}Mg_{0.54}Zr_{0.51}O_{19}$	$SrGa_{7.99}Al_{3.17}Mg_{0.43}Zr_{0.40}O_{19}$
XRF/ICP-OES	$Sr_{1.03}Ga_{10.81}Mg_{0.58}Zr_{0.58}O_{18.99}$[18]	$Sr_{0.913}Ga_{7.626}Al_{2.991}Mg_{0.428}Zr_{0.411}O_{20.689}$

sites follows the trend dictated by the defect formation energies, being the first and second lowest. Furthermore, the composition obtained agrees well with the values obtained through the chemical analysis and again reflects the slightly increased Mg/Zr-ratio as already observed in SGMZ. The slight undersaturation of Mg and Zr and corresponding oversaturation of Al can likely be relegated to segregation effects during growth.

7 Conclusions

In our study, we were able to elucidate the structure of the chemically altered magnetoplumbite-type Mg,Zr:$Sr(Ga_{12-x}Al_x)O_{19}$ solid solution. Both single crystal diffraction and HAXPES methods were used in synergy with DFT modeling to understand both the structure of the investigated material as well as its formation on a fundamental atomistic level.

The formation energies obtained through DFT predict the energetically most beneficial sites for the various substituents to occupy. In the case of Mg and Zr, this is the $4f_1$ and $4f_2$ sites, respectively, which agrees well with the structural fit of the single crystal XRD data for both SGMZ and SGAMZ. As for Al, in the case of an SGAMZ solid solution, the formation energies dictate an order, in which the trivalent Wyckhoff-sites are occupied. Here, the *2a* site has the highest probability to be populated by this element, followed by both the *12k* and $4f_2$ site, which is in accordance with E^f_{Al} being the 2nd and 3rd lowest for these two sites. In the investigated crystal, Al occupancy follows this order as shown by the experimental data, thus again establishing congruence between the theoretical predictions and the structural fit. Identification of the lattice site of substitutional cations is a first step towards providing a powerful and predictive framework for understanding cation ordering in complex magnetoplumbite-type oxides. The results presented as well as the scientific approach therefore provide a robust basis for customizing the investigated magnetoplumbite-type compound by chemical substitution.

Further investigations will focus on thermodynamic quantities (e.g., C_p, thermal conductivity) dependence on the Al/Ga ratio. Beyond that, our further efforts aim at establishing routes of also increasing the lattice parameter of SGMZ through cationic substitution.

Acknowledgments: We acknowledge the use of the Bruker D8 Venture 4-circle single crystal X-ray diffractometer at the University of Bremen. The device was used to measure all the XRD data pertaining SGMZ presented in this publication. Furthermore, the authors acknowledge and are very grateful for the financial support through the MAPEX Core Facility which funded the measurement campaign for a duration of three weeks. The SGAMZ data presented was measured at the Bruker D8 Venture 4-circle single crystal X-ray diffractometer at the chemical faculty of the Humboldt University Berlin, for which we fully acknowledge and are grateful for the support of Dr. Beatrice Cula. The authors gratefully acknowledge the financial support by the Deutsche Forschungsgemeinschaft (DFG) through the research group FOR5044 (ID: 426703838; https://www.FOR5044.de). Calculations for this research were performed on the Lichtenberg high-performance computer of the TU Darmstadt. The authors furthermore acknowledge the computational resources provided by the HPC Core Facility and the HRZ of the Justus-Liebig-Universität Gießen. Parts of this research were carried out at PETRA III using beamline P22. Beamtime was allocated for proposal I-20231120. Funding for the HAXPES instrument at beamline P22 by the Federal Ministry of Education and Research (BMBF) under contracts 05KS7UM1 and 05K10UMA with Universität Mainz, 05KS7WW3, 05K10WW1 and 05K13WW1, also the Universität Würzburg is gratefully acknowledged.

Research ethics: Not applicable.

Informed consent: Not applicable.

Author contributions: All authors have accepted responsibility for the entire content of this manuscript and approved its submission.

Use of Large Language Models, AI and Machine Learning Tools: None declared.

Conflict of interest: The authors state no conflict of interest.

Research funding: None declared.

Data availability: The datasets generated during and/or analysed during the current study are available in the CCDC / FIZ Karlsruhe repository, Deposition numbers 2577327 and 2577328.

References

1. Narayan, J. New Frontiers in Thin Film Growth and Nanomaterials. *Metall. Mater. Trans. B* **2005**, *36*, 5–22.
2. Seredyński, B.; Ogorzałek, Z.; Zajkowska, W.; Bożek, R.; Tokarczyk, M.; Suffczyński, J.; Kret, S.; Sadowski, J.; Gryglas-Borysiewicz, M.; Pacuski, W. Molecular Beam Epitaxy of a 2D Material Nearly Lattice Matched to a 3D Substrate: $NiTe_2$ on GaAs. *Cryst. Growth Des.* **2021**, *21* (10), 5773–5779.
3. Itagaki, N.; Nakamura, Y.; Narishige, R.; Takeda, K.; Kamataki, K.; Koga, K.; Hori, M.; Shiratani, M. Growth of Single Crystalline Films on Lattice-Mismatched Substrates Through 3D to 2D Mode Transition. *Sci. Rep.* **2020**, *10*, 4669.
4. Tang, S.-J.; Lee, C.-Y.; Huang, C.-C.; Chang, T.-R.; Cheng, C.-M.; Tsuei, K.-D.; Jeng, H.-T.; Yeh, V.; Chiang, T. C. Electronic Versus Lattice Match for Metal-Semiconductor Epitaxial Growth: Pb on Ge(111). *Phys. Rev. Lett.* **2011**, *107*, 066802.
5. Sowadski, L.; Anderson, S.; Lerch, C.; Medvedeva, J.; Vojta, T. Magnetic Properties of Diluted Hexaferrites. *Phys. Rev. B* **2024**, *110*, 014432.
6. Bing Kong, L.; Liu, L.; Yang, Z.; Li, S.; Zhang, T.; Wang, C. Theory of Ferrimagnetism and Ferrimagnetic Metal Oxides. In *Magnetic, Ferroelectric, and Multiferroic Metal Oxides*; Elsevier: Oxford, 2018.
7. Smart, M. M.; Smith Pellizzeri, T. M.; Morrison, G.; McMillen, C. D.; zur Loye, H.-C.; Kolis, J. W. Ferrite Materials Containing Kagomé Layers: Chemistry of $Ba_2Fe_{11}Ge_2O_{22}$ and $K_2Co_4V_9O_{22}$ Hexaferrites. *Chem. Mater.* **2021**, *33* (7), 2258–2266.
8. Joshi, R. S.; Kumar, P. S. A. Magnetic Solid-State Materials. In *Comprehensive Inorganic Chemistry II*; Elsevier: Oxford, 2013.
9. Wang, P. S.; Xiang, H. J. Room-Temperature Ferrimagnet with Frustrated Antiferroelectricity: Promising Candidate Toward Multiple-State Memory. *Phys. Rev. X* **2014**, *4* (1), 011035.
10. Pullar, R. C. Hexagonal Ferrites: A Review of the Synthesis, Properties and Applications of Hexaferrite Ceramics. *Prog. Mater. Sci.* **2012**, *57* (7), 1191–1334.
11. Schlom, D. G.; Chen, L.-Q.; Fennie, C. J.; Gopalan, V.; Muller, D. A.; Pan, X.; Ramesh, R.; Uecker, R. Elastic Strain Engineering of Ferroic Oxides. *MRS Bull.* **2014**, *39* (2), 118–130.

12. Klimm, D.; Szczefanowicz, B.; Wolff, N.; Bickermann, M. Phase Diagram Studies for the Growth of (Mg,Zr):$SrGa_{12}O_{19}$ Crystals. *J. Therm. Anal. Calorim.* **2021**, 1–7. https://doi.org/10.1007/s10973-021-11050-4.
13. Haberey, F.; Leckebusch, R.; Rosenberg, M.; Sahl, K. Epitaxial Growth and Properties of Strontium Hexaaluminoferrite Layers. *J. Cryst. Growth* **1981**, *52*, 734–737.
14. Harikrishnan, K. P.; Li, Y. E.; Shao, Y.-T.; Chen, Z.; Yan, J.; Guguschev, C.; Schlom, D. G.; Muller, D. A. Polar Nano-Domains in Barium Hexaferrite Revealed with Multislice Electron Ptychography. *Microsc. Microanal.* **2022**, *28* (S1), 476–478.
15. Kimura, K.; Ohgaki, M.; Tanaka, K.; Morikawa, H.; Marumo, F. Study of the Bipyramidal Site in Magnetoplumbite-Like Compounds, $SrM_{12}O_{19}$ (M= Al, Fe, Ga). *J. Solid State Chem.* **1990**, *87* (1), 186–194.
16. Li, J.; Medina, E. A.; Stalick, J. K.; Sleight, A. W.; Subramanian, M. A. Structural Studies of $CaAl_{12}O_{19}$, $SrAl_{12}O_{19}$, $La_{2/3+\delta}Al_{12-\delta}O_{19}$, and $CaAl_{10}NiTiO_{19}$ with the Hibonite Structure; Indications of an Unusual Type of Ferroelectricity. *Z. Naturforsch. B* **2016**, *71* (5), 475–484.
17. Guguschev, C.; Richter, C.; Brützam, M.; Dadzis, K.; Hirschle, C.; Gesing, T. M.; Schulze, M.; Kwasniewski, A.; Schreuer, J.; Schlom, D. G. Revisiting the Growth of Large (Mg,Zr):$SrGa_{12}O_{19}$ Single Crystals: Core Formation and Its Impact on Structural Homogeneity Revealed by Correlative X-ray Imaging. *Cryst. Growth Des.* **2022**, *22* (4), 2557–2568.
18. Mateika, D.; Laurien, R. Czochralski Growth of Solid Solutions of Strontium Hexagallate with Magnesium and Zirconium as Dopants. *J. Cryst. Growth* **1981**, *52*, 566–572.
19. Sheldrick, G. M. A Short History of SHELX. *Acta Crystallogr., Sect. A: Found. Crystallogr.* **2008**, *64* (1), 112–122.
20. Dolomanov, O. V.; Bourhis, L. J.; Gildea, R. J.; Howard, J. A. K.; Puschmann, H. OLEX2: A Complete Structure Solution, Refinement and Analysis Program. *J. Appl. Crystallogr.* **2009**, *42* (2), 339–341.
21. Schlueter, C.; Gloskovskii, A.; Ederer, K.; Schostak, I.; Piec, S.; Sarkar, I.; Matveyev, Y.; Lömker, P.; Sing, M.; Claessen, R. The New Dedicated HAXPES Beamline P22 at PETRA III. *AIP Conf. Proc.* **2019**, *2054* (1).
22. Müller, M.; Lömker, P.; Rosenberger, P.; Hussein Hamed, M.; Mueller, D. N.; Heinen, R. A.; Szyjka, T.; Baumgarten, L. Hard X-ray Photoelectron Spectroscopy of Tunable Oxide Interfaces. *J. Vac. Sci. Technol. A* **2022**, *40* (1). https://doi.org/10.1116/6.0001491.
23. Kresse, G.; Furthmüller, J. Efficiency of Ab-Initio Total Energy Calculations for Metals and Semiconductors Using a Plane-Wave Basis Set. *Comput. Mater. Sci.* **1996**, *6* (1), 15–50.
24. Kresse, G.; Furthmüller, J. Efficient Iterative Schemes for Ab Initio Total-Energy Calculations Using a Plane-Wave Basis Set. *Phys. Rev. B* **1996**, *54* (16), 11169.
25. Blöchl, P. E. Projector Augmented-Wave Method. *Phys. Rev. B* **1994**, *50* (24), 17953.
26. Kresse, G.; Joubert, D. From Ultrasoft Pseudopotentials to the Projector Augmented-Wave Method. *Phys. Rev. B* **1999**, *59* (3), 1758.
27. Monkhorst, H. J.; Pack, J. D. Special Points for Brillouin-Zone Integrations. *Phys. Rev. B* **1976**, *13*, 5188–5192.
28. Feynman, R. P. Forces in Molecules. *Phys. Rev.* **1939**, *56*, 340–343.
29. Perdew, J. P.; Zunger, A. Self-Interaction Correction to Density-Functional Approximations for Many-Electron Systems. *Phys. Rev. B* **1981**, *23*, 5048–5079.
30. Perdew, J. P.; Burke, K.; Ernzerhof, M. Generalized Gradient Approximation Made Simple. *Phys. Rev. Lett.* **1996**, *77*, 3865–3868.
31. Perdew, J. P.; Ruzsinszky, A.; Csonka, G. I.; Vydrov, O. A.; Scuseria, G. E.; Constantin, L. A.; Zhou, X.; Burke, K. Restoring the Density-Gradient Expansion for Exchange in Solids and Surfaces. *Phys. Rev. Lett.* **2008**, *100*, 136406.
32. Murnaghan, F. D. The Compressibility of Media Under Extreme Pressures. *Proc. Natl. Acad. Sci. U. S. A.* **1944**, *30*, 244–247.
33. Van de Walle, C. G.; Neugebauer, J. First-Principles Calculations for Defects and Impurities: Applications to III-Nitrides. *J. Appl. Phys.* **2004**, *95* (8), 3851–3879.
34. Freysoldt, C.; Neugebauer, J.; Van de Walle, C. G. Fully Ab Initio Finite-Size Corrections for Charged-Defect Supercell Calculations. *Phys. Rev. Lett.* **2009**, *102*, 016402.
35. https://winter.group.shef.ac.uk/webelements/ (accessed 2025-09-23).
36. Scofield, J. H. Theoretical Photoionization Cross Sections from 1 to 1500 keV. Technical report; California Univ., Lawrence Livermore Lab.: Livermore, 1973.
37. Trzhaskovskaya, M. B.; Yarzhemsky, V. G. Dirac–Fock Photoionization Parameters for HAXPES Applications. *Atomic Data Nucl. Data Tables* **2018**, *119*, 99–174.
38. Rehm, O.; Baumgarten, L.; Guido, R.; Düring, P. M.; Gloskovskii, A.; Schlueter, C.; Mikolajick, T.; Schroeder, U.; Müller, M. Long-Term Stability and Oxidation of Ferroelectric AlScN Devices: An Operando Hard X-ray Photoelectron Spectroscopy Study. *Phys. Status Solidi RRL-Rapid Res. Lett.* **2025**, *19* (3), 2400307.
39. Szyjka, T.; Baumgarten, L.; Rehm, O.; Richter, C.; Matveyev, Y.; Schlueter, C.; Mikolajick, T.; Schroeder, U.; Müller, M. From Doping to Dilution: Local Chemistry and Collective Interactions of La in HfO_2. *Phys. Status Solidi RRL-Rapid Res. Lett.* **2022**, *16* (10), 2100582.